200 *Chem. Mater.* **2011,** *23,* 200–207
DOI:10.1021/cm1028782

CHEMISTRY OF MATERIALS
Article

Zn-Doped RuO_2 electrocatalyts for Selective Oxygen Evolution: Relationship between Local Structure and Electrocatalytic Behavior in Chloride Containing Media

Valery Petrykin,*,† Katerina Macounova,† Jiri Franc,† Oleg Shlyakhtin,‡ Mariana Klementova,§ Sanjeev Mukerjee,⊥ and Petr Krtil*,†

†*J. Heyrovsky Institute of Physical Chemistry, Academy of Sciences of the Czech Republic, v.v.i, Dolejskova 3, 18223 Prague, Czech Republic,* ‡*Department of Chemistry, Moscow State University, 117899 Moscow, Russia,* §*Institute of Inorganic Chemistry, Academy of Sciences of the Czech Republic, vvi Rez, 25263 Prague, Czech Republic, and* ⊥*Depratment of Chemistry and Chemical Biology, Northeastern University, 360 Huntington Avenue, Boston, Massachusetts, United States*

Received October 6, 2010. Revised Manuscript Received December 7, 2010

Nanocrystalline electrocatalytically active materials of chemical composition $Ru_{1-x}Zn_xO_2$ ($0 < x < 0.3$) were synthesized by freeze-drying technique. The diffraction patterns of the prepared samples corresponded to single-phase rutile type oxides. Local structure of the $Ru_{1-x}Zn_xO_2$ based on refinement of Ru K and Zn K edge EXAFS functions shows clustering of the Zn ions in the blocks with ilmenite structure intergrowing with Ru-rich rutile blocks. $Ru_{1-x}Zn_xO_2$ oxides are selective catalysts for anodic oxygen evolution. The selectivity toward oxygen evolution in the presence of chlorides is affected by the actual Zn content and can be ascribed to structural hindrance of the formation of the surface peroxo group based active sites for chlorine evolution. The selectivity toward oxygen evolution in presence of chlorides is accompanied by the drop of the total activity, which gets more pronounced with increasing Zn content.

Introduction

The electrochemistry of anodic oxygen evolution reaction (OER) as well as the cathodic process of oxygen reduction represent the major challenges of modern electrocatalysis. The interest in both types of processes is fuelled by the importance of the practical applications, which include fuel cells,[1] (photo-) electrochemical water splitting,[2] or technical electrolysis in chlor-alkali industry.[3] Although the oxygen reduction seems to be so far best controlled on metal electrocatalysts, the oxygen evolution proceeds only on oxide type surfaces. Rutile type conducting oxides such as RuO_2 or IrO_2 are industrial benchmark anode materials because of their outstanding chemical stability and remarkable electrocatalytic activity. One of the remaining issues of this type of catalysts is relatively poor selectivity toward oxygen evolution if the electrolyzed solution contains chlorides. The systematic theoretical approach to qualify the electrocatalytic processes on the rutile type oxides in oxygen and chlorine evolution reactions (CER) was presented by Rossmeisl and co-workers.[4,5] The density functional theory (DFT)-based thermodynamic analysis predicts that both electrode processes are strongly correlated on rutile type oxide surfaces. In the case of oxygen evolution, it is stated that the process proceeds preferentially via surface peroxide-route[4] when the formation of the surface oxo- or peroxo- species represents the rate-limiting step. Extending the same DFT approach to chlorine evolution process one finds that the surface peroxo-groups simultaneously act as the active sites in chlorine evolution. Therefore, the presence of chlorides alters the selectivity of the rutile type surface from oxygen evolution process toward chlorine evolution as a result of the competition between both processes for the same surface active site. In addition to the effects of pH and chloride concentration, the selectivity of the oxide surface is also influenced by the electronic properties of the electrocatalysts, which are in the given theoretical model represented by oxygen adsorption energy.[4,5] In the case of RuO_2-based systems when oxygen adsorption energy nears 2 eV, it is predicted that the selectivity of the surface toward chlorine evolution results from the oxidative attack of the Cl^- on the surface peroxo groups connecting two Ru atoms along [001] direction. It has to be noted, however, that the results of the theoretical calculations are restricted to the processes proceeding on crystal faces and do not account for reactivity of the sites with lower dimensionality (e.g., crystal edges, vertices, or defects), which may play a significant role in real nanocrystalline catalysts.[6]

*Corresponding author. E-mail: Valery.Petrykin@jh-inst.cas.cz (V.P.); Petr.Krtil@jh-inst.cas.cz (P.K.) Phone: +420.266053826. Fax: +420-286582307.

(1) Simon, B.; Karl, M.; Mayrhofer, J. J; Ross, P. N.; Markovic, N. M.; Rossmeisl, J.; Greeley, J.; Nørskov, J. K *Angew. Chem., Int. Ed.* **2006**, *45*, 2897.
(2) Kanan, M. W.; Nocera, D. G. *Science* **2008**, *321*, 1072.
(3) Trasatti, S. *Electrochim. Acta* **2000**, *45*, 2377.
(4) Rossmeisl, J.; Qu, Z. W.; Zhu, H.; Kroes, G. J.; Norskov, J. K. *J. Electroanal. Chem.* **2007**, *607*, 83.
(5) Hansen, H. A.; Man, I. C.; Studt, F.; Abild-Pedersen, F.; Bligaard, T.; Rossmeisl, J. *Phys. Chem. Chem. Phys.* **2010**, 283.

 Published on Web 12/28/2010

The results of this theoretical analysis seem to be countered by the behavior of the ruthenium oxides with heterovalent substitution with Co,[7] Ni,[8] Fe,[9] and particularly of Zn-doped RuO_2.[10] We recently reported[10] on the surprisingly high selectivity of Zn-doped RuO_2 (RuO_2:Zn) electrocatalysts toward oxygen evolution in the chloride containing media. These materials are of an interest from both fundamental and practical points of view, because they explore the region addressed inadequately in the theoretical models and show promise for the direct splitting of seawater. The high selectivity of Zn-doped materials for the oxygen evolution has not yet been satisfactorily explained and was tentatively ascribed to modification of the local structure on the length scale of ca. 3−4 Å. Indeed, the extended X-ray absorption fine structure (EXAFS) functions extracted for RuO_2:Zn materials revealed that the presence of Zn in the lattice resulted in a significant rearrangement of crystal structure in the vicinity of Zn cation,[10] and that the local structure was clearly different from the local structure of the other doped RuO_2-based catalysts.[11] Despite the promising material's behavior, the local structure of RuO_2:Zn remains unknown, and its relationship with the material properties is still missing. The local structure of the RuO_2:Zn electrocatalysts is one of the key issues addressed in this paper, which focuses on the details of the synthesis of this class of materials, reports on the real structure of Zn doped RuO_2 nanocrystalline materials and relates the local structure to observed electrocatalytic behavior in oxygen and parallel oxygen and chlorine evolution processes.

Experimental Section

Synthesis of $Ru_{1-x}Zn_xO_2$. The samples of the general composition of $Ru_{1-x}Zn_xO_2$ (x = 0.05−0.30) were synthesized by the freeze-drying method based on the procedure described in ref 10. The flowchart of the synthesis procedures is presented as Supporting Information. Typically the Ru nitrosyl nitrate ($Ru(NO)(NO_3)_x(OH)_y$ Alfa Aesar, 31.3% Ru), and Zn-$(CH_3COO)_2$•$2H_2O$ (ACS grade, Wako) were used. The actual amount of water in the crystal hydrate was determined by thermogravimetry. First 0.03 M zinc acetate stock solution was prepared, by dissolving $Zn(CH_3COO)_2 \cdot 2H_2O$ in water. Simultaneously, the appropriate amount of Ru nitrosyl nitrate was dissolved in 50 mL of water at 30 °C to obtain 0.01 M solution. After dissolution of Ru nitrosyl nitrate, stoichiometric amounts of Zn acetate stock solutions were added to obtain the required Ru and Zn ratio. After stirring for 5−10 min the solution volume was adjusted to 100 mL and these solutions were sprayed into liquid N_2. The ice samples were transferred onto the metal trays and put into the precooled freeze-dryer. The following lyophilization program was used: −30 °C (1 h), −25 °C (3 h), −20 °C (4 h), −15 °C (6 h), and −30 °C (5 h). The samples were, after drying, inserted into a furnace preheated at 400 °C and annealed for 2 hours. The samples were then removed from the furnace and cooled down to room temperature in the air.

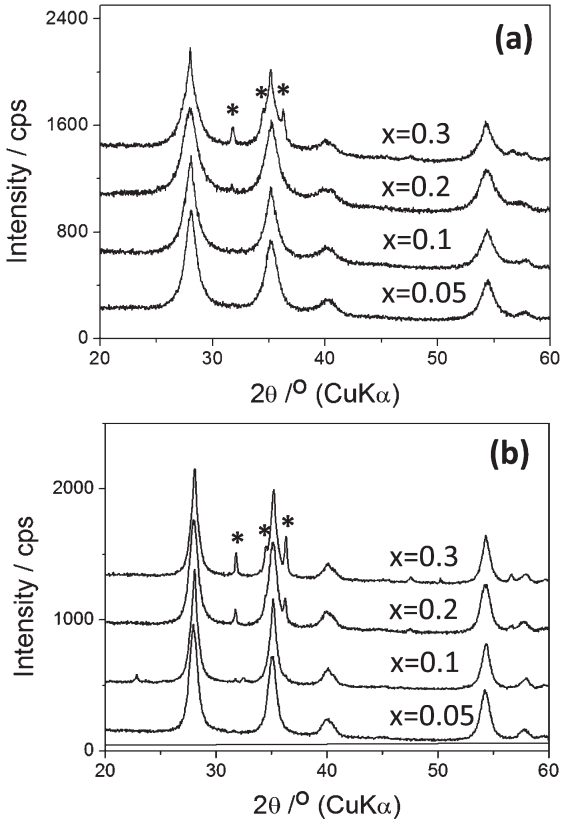

Figure 1. Powder X-ray diffraction patterns of nanocrystalline $Ru_{1-x}Zn_xO_2$ ($0.05 \leq x \leq 0.3$) materials after annealing at (a) 400 and (b) 600 °C for 2 h. Asterisks mark reflections of ZnO phase.

Characterization. Thermal analysis of freeze-dried precursors and starting reagents was performed at heating rates of 2 deg/min (20 °C − 400 °C) and 5 deg/min (400 °C − 700 °C) in air at 30 cm^3/min flow rate using Pyris Diamond TG/DTA (Perkin-Elmer) thermal analyzer. Typically, 1.5−4 mg samples of powders were analyzed using Pt sample crucible. The phase composition of the samples was characterized by a Bruker D8 Advance powder X-ray diffractometer with Vantec-1 detector and $Cu_{K\alpha}$ radiation operating at 40 kV-30 mA in the scanning mode with a scanning rate of 1°/min (Figure 1). The bulk chemical composition of the prepared materials was analyzed using X-ray energy dispersive spectroscopy using Hitachi S4800 scanning electron microscope (SEM) equipped with a Nanotrace EDX detector (Thermo Electron). Transmission electron microscopy (TEM) studies (Figure 2) were performed with a JEM-3010 (JEOL) instrument operating at 300 kV. The $Ru_{1-x}Zn_xO_2$ powders were dispersed in ethanol using ultrasonic bath. A drop of the obtained solution was transferred onto a Cu microgrid coated with holey carbon film and allowed to dry under ambient conditions. The materials structure and chemical composition was confirmed by electron diffraction and EDX analysis.

The X-ray absorption spectroscopy (XAS) was used to gather information on local structures of the materials in the vicinity of both Ru and Zn atoms. X-ray near edge absorption spectra (XANES) and extended X-ray absorption fine structure (EXAFS) data were collected on pellets containing approximately 30 mg of

(6) Jirkovsky, J.; Hoffmannova, H.; Klementova, M.; Krtil, P. *J. Electrochem. Soc.* **2006**, *153*, E111.
(7) Makarova, M.; Jirkovsky, J.; Klementova, M.; Jirka, I.; Macounova, K.; Krtil, P. *Electrochim. Acta* **2008**, *53*, 5626.
(8) Macounova, K.; Makarova, M.; Jirkovsky, J.; Franc, J.; Krtil, P. *Electrochem. Solid-State Lett.* **2008**, *11*, F28.
(9) Macounova, K.; Makarova, M.; Jirkovsky, J.; Franc, J.; Krtil, P. *Electrochim. Acta* **2008**, *53*, 6126.
(10) Petrykin, V.; Macounová, K.; Shlyakhtin, O.; Krtil, P. *Angew. Chem., Int. Ed.* **2010**, *49*, 4813.
(11) Petrykin, V.; Bastl, Z.; Franc, J.; Macounova, K.; Makarova, M.; Mukerjee, S.; Ramaswamy, N.; Spirovova, I.; Krtil, P. *J. Phys. Chem. C* **2009**, *113*, 21657.

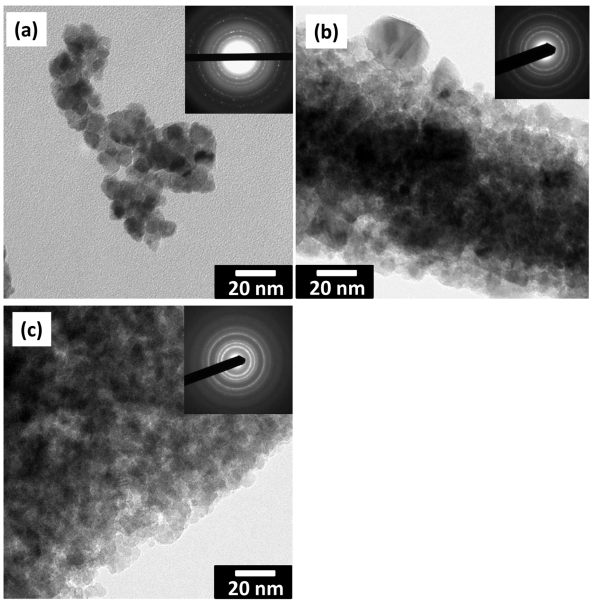

Figure 2. TEM micrographs of nanocrystalline $Ru_{1-x}Zn_xO_2$ materials after annealing at 400 °C with (a) $x = 0.05$; (b) $x = 0.1$, and (c) $x = 0.2$. Electron diffraction patterns in insets correspond to rutile type crystal structure.

$Ru_{1-x}Zn_xO_2$ in 200 mg of boron nitride (Aldrich, ACS grade). The XANES and EXAFS spectra were measured at the X18B beamline (Si(111) monochromator) of the National Synchrotron Light Source (Brookhaven National Laboratory, USA). The spectra were measured in transmission mode at Ru K edge (22117 eV) and Zn K absorption edge (9659 eV). The Zn K edge spectra of the sample with $x = 0.05$ were acquired in fluorescence mode using a 13 channel Ge detector. Each spectrum was recorded at three different scanning step sizes: pre-edge region from 200 to 30 eV was scanned in 5 eV steps to enable background subtraction; in the 30 eV pre-edge and 30 eV postedge range the step size of 0.5 eV was used to acquire XANES part of the spectra, whereas the EXAFS data extending up to 16 $Å^{-1}$ in the k-space were collected with the variable step size corresponding to 0.05 $Å^{-1}$.

The preliminary data handling, normalizations, and extraction of the extended X-ray absorption fine structure (EXAFS) functions were performed in the IFEFFIT software package.[12] The photoelectron wave vector k for the Fourier transform of spectra was kept within the range of $k = 3.5-15.5$ $Å^{-1}$ for Ru-EXAFS and $k = 2-13.1$ $Å^{-1}$ for Zn-EXAFS. The k-weighting factor of 2 was applied. The EXAFS functions are presented in R space in the range of $R = 1-6$ Å. The full-profile refinement of the EXAFS spectra by nonlinear least-squares (NLLS) minimization in the R-space with k-weighting factor equal to 3 was carried out using Artemis program of the IFEFFIT package (see Figure 3−6). The theoretical models were generated using FEFF6.2 library.

The electrodes for electrochemical experiments were prepared from synthesized $Ru_{1-x}Zn_xO_2$ materials by sedimentation of nanocrystalline powder from a water based suspension on Ti mesh (open area 20%, Goodfellow). The duration of the deposition was adjusted to obtain the surface coverage of about 1−2 mg/cm^2 of active oxide. The deposited layers were stabilized by annealing the electrodes for 20 min at 400 °C in air. The initial oxide suspensions were prepared in an ultrasound bath and contained approximately 5 g/L of $Ru_{1-x}Zn_xO_2$ in Milli-Q quality deionized water.

(12) Neville, M. *J. Synchrotron Radiat*. **2001**, *8*, 322.

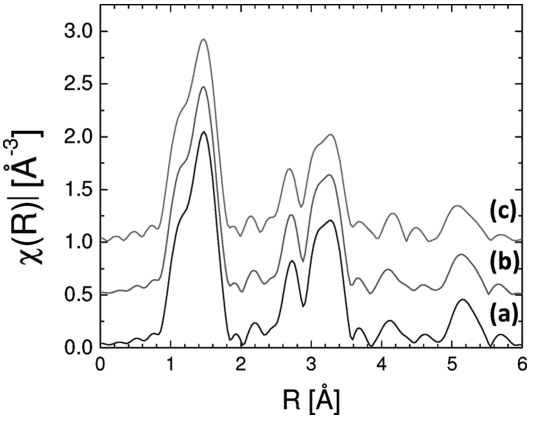

Figure 3. k^2-normalized RuK edge EXAFS functions of $Ru_{1-x}Zn_xO_2$: (a) $x = 0.05$, (b) $x = 0.10$, and (c) $x = 0.2$. Phase correction was not applied.

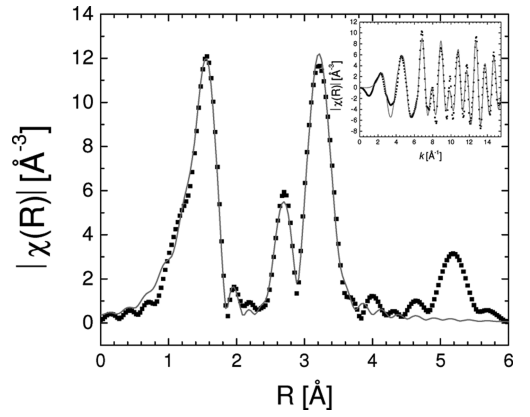

Figure 4. k^3-normalized Ru-EXAFS function of $Ru_{1-x}Zn_xO_2$ $x = 0.2$ (square) and result of fitting using RuO_2 structure as a model. Inset shows the results of fitting in k-space. Phase correction was not applied.

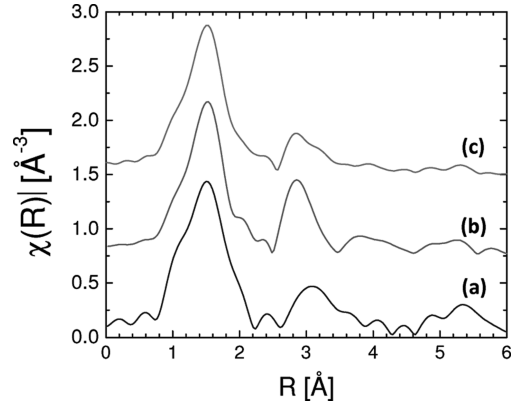

Figure 5. k^2-normalized ZnK edge EXAFS functions of $Ru_{1-x}Zn_xO_2$: (a) $x = 0.05$, (b) $x = 0.10$, and (c) $x = 0.2$. Phase correction was not applied.

The electrochemical behavior of the RuO_2:Zn electrocatalysts was studied by cyclic voltammetry combined with differential electrochemical mass spectroscopy (DEMS). All experiments were performed in a homemade Kel-F single compartment cell. The experiments were performed in a three electrode arrangement using a PAR 263A potentiostat. Pt and Ag/AgCl were used as an auxiliary and a reference electrode, respectively. The activity of the prepared materials in both oxygen and chlorine evolution reactions was studied in 0.1 M $HClO_4$ (Aldrich, p.a.) containing variable amount of NaCl (Aldrich, ACS grade) corresponding

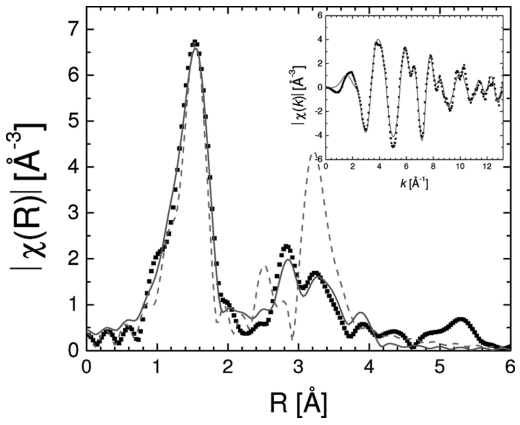

Figure 6. k^3-normalized Zn-EXAFS function of $Ru_{1-x}Zn_xO_2$, $x = 0.2$ (square), simulation based on refined RuO_2 structure as a model (dash line) and refinement result using ilmenite as a structural model. Inset shows the results of fitting in k-space for "$RuZnO_3$" ilmenite. Phase correction was not applied.

to concentrations between 0.01 and 0.3 M. The DEMS apparatus consisted of Prisma QMS200 quadrupole mass spectrometer (Balzers) connected to TSU071E turbomolecular drag pumping station (Balzers).

Results and Discussion

The thermal analysis data of Ru nitrosyl nitrate, Zn acetate and freeze-dried precursor containing Ru and Zn ions (see the Supporting Information) show that thermal decomposition of Ru nitrosyl nitrate starts below 100 °C by the loss of water. This step is completed by 150 °C. The second stage of decomposition takes place at temperatures above 200 °C and completes at ~350 °C. Decomposition of Zn acetate occurs at lower temperature than Ru nitrosyl nitrate, and constant mass of the sample is achieved already at 260 °C. The decomposition of the freeze-dried precursors for $Ru_{1-x}Zn_xO_2$ resembles the decomposition process of the Ru nitrosyl nitrate. The presence of Zn acetate in the precursor, however, shifts the decomposition to higher temperatures. Such a thermal behavior of freeze-dried powders, when the decomposition temperature of the precursor is higher than those of individual compounds, points out to a formation of a solid solution including both Ru and Zn ions in the ice. On the basis of the results of TG analysis, the temperature of the heat treatment of the powder was chosen to be 400 °C, which guarantees complete decomposition of the precursor and provides thermal conditions consistent with the annealing regime used in syntheses of the other RuO_2-based nanocrystalline materials[7−9] prepared by coprecipitation method.

All samples of $Ru_{1-x}Zn_xO_2$ ($0.05 \le x \le 0.2$) annealed at 400 °C were of single phase character (see Figure 1a) according to the results of the analysis of the powder XRD data. The reflection positions as well as intensities of those diffraction peaks matched RuO_2 PDF file 431027. The peak width of the synthesized materials corresponded to the average coherent domain size of 8−12 nm, which agrees well with TEM data. Annealing at 600 °C results in the formation of ZnO impurity in the nanocrystalline materials with Zn content as low as 10 mol %, (see Figure 1b).

The TEM micrographs in Figure 2 show the typical microstructures of the $Ru_{1-x}Zn_xO_2$ ($x = 0.05$, 0.10 and 0.20) materials. One may notice that the powders are composed of 5−10 nm particles with rather uniform size distribution. The size of the particles slightly decreases with the increase of Zn concentration. The selected area electron diffraction patterns correspond to a single phase with rutile type structure identical to RuO_2.

The local structure of the $Ru_{1-x}Zn_xO_2$ electrocatalysts was resolved from XAFS data measured at RuK- and ZnK edges. It has to be noted that local structure characterization bears high relevance to the catalytic behavior in contrast to, e.g. diffraction data, since the catalytic activity is determined on the length-scale comparable with molecular dimensions, i.e., 2−5 Å. Figure 3 presents Fourier transformed EXAFS functions extracted from RuK edge data plotted in the R-space to emphasize the chemically relevant information. The Ru-EXAFS functions resemble those of nondoped RuO_2, which were discussed in detail in ref 11. According to ref 11, one can assign the first peak at 1.95−2.00 Å to the scattering of photoelectrons by oxygen atoms forming RuO_6 octahedra. The second strong peak at ~3.0−3.1 Å originates mainly from the scattering process involving Ru−Ru path along the c axis of RuO_2 crystal. The next strong peak at 3.5−3.7 Å includes contributions from several scattering paths, whereas its main component reflects Ru−Ru coordination along the body diagonal of RuO_2 unit cell. As one may notice from the set of Ru-EXAFS functions in Figure 3, introduction of Zn into RuO_2 does not lead to significant changes of the local environment of Ru atoms because position of the peaks and their relative magnitude remain constant. To reveal possible finer changes in the local structure resulting from Zn substitution, we carried out the full-profile refinement of the RuK edge data. To stress possible changes in the metal−metal coordination environment, we used a k^3-weighting scheme to enhance relative contribution from the longer scattering paths.

The refined model included all single scattering and the multiple scattering events with the relative amplitude exceeding 7%. The refinement procedure consisted of three stages. First, the initial structure was allowed to expand isotropically and the values of amplitude, phase shift ΔE_0, and Debye−Waller (DW) factors for cations and anions were refined. The amount of Zn ions in each Ru site was assumed to be 0.2 as expected from overall stoichiometry. During the next step, the isotropic expansion−contraction was kept only for oxygen atoms in the first coordination shell, whereas the distances from the core cation to other cations were allowed to change independently. The final stage of the refinement included releasing the occupancies of Zn and Ru site while keeping constraints on the total occupancy (equal to 1) and fraction of each metal in the particular site (attaining only positive values). Details of the refinement procedure strategy were described in ref 11. The comparison of the experimental Ru-EXAFS function and the theoretical curve for the refined model is provided in Figure 4. The refined values of the effective scattering paths, Debye−Waller factors, amplitudes, and phase shifts are

Table 1. Selected Refined Interatomic Distances and Corresponding Debye−Waller Factors for RuO_2 Obtained by Fitting the k^3-Normalized Fourier Transformed EXAFS Function Extracted from Ru K edge (22117 eV) X-ray Absorption Spectrum[a]

			bond length (Å)		
path	CN	occupancy	RuO^2 in ref 11	refined	DW (Å^2)
Ru−O	2	1	1.921	1.928(4)	0.0035(8)
Ru−O	4	1	1.983	1.990(4)	0.0035(8)
Ru−Ru	2	0.92	3.109	3.106(6)	0.0041(4)
Ru−Zn	2	0.08(12)		3.137(10)	0.0008(4)
Ru−Ru	8	0.89	3.544	3.542(6)	0.0057(14)
Ru−Zn	8	0.11(4)		3.482(30)	0.0008(4)

[a] *R*-factor = 0.00751, *k* range 3.5−15.5 Å^{-1}, *R* range 1−4 Å, amplitude = 1.008, E_0 = −2.921 eV.

summarized in Table 1. According to the data shown in Table 1, the substitution of Ru ions by Zn has very little effect on the Ru−O distances in the first coordination shell. This is consistent with assumption that the oxidation state of Ru does not change due to Zn incorporation. Accordingly, the positions of RuK edge in XANES parts of the spectra of pure and Zn doped RuO_2 are identical within the resolution of the data acquisition (see the Supporting Information). With respect to metal−metal distances, the Ru−Zn bonds are significantly longer than Ru−Ru bonds, which reflects the differences in ionic radii of Ru^{4+}(0.62 Å) and Zn^{2+}(0.74 Å).[13] Surprisingly, the refinement of Zn/Ru occupancies in lattice sites within the rutile type structural model returned values lower than those predicted from average chemical composition. In particular, Zn ions are almost absent in the closest metal−metal coordination shell and only half of expected amount was found in the second closest metal coordination shell. Although refinement of the coordination numbers from the EXAFS data is not extremely accurate, this information in the combination with interatomic distances and absence of changes in the shape of Ru-EXAFS function with the change of Zn concentration leads to a conclusion that the largest fraction of Zn atoms is segregated in the relatively small Zn-rich areas.

This seems to be supported by Zn-EXAFS data presented in Figure 5. The extracted EXAFS functions do not resemble those recorded on the RuK edge. The local environment of Zn atoms is significantly departed from that of the rutile structure, mainly as far as the metal−metal coordination is concerned. The results of refinement of local structure around Zn ions based on the collected Zn-EXAFS data are summarized in Figure 6. The refinement procedure could not be based on the same model as used in Ru-EXAFS function refinement since simulated EXAFS function deviates strongly from the experimental data (see dashed curve in Figure 6) and reasonable agreement could not be achieved by variation of the available parameters (metal−metal distances, DW factors and occupancies of the corresponding metal sites). The refinement of Zn-EXAFS data using the model based on rutile structure converges to a local structure featuring reversed coordination numbers in the first and the second Zn^- metal coordination shells. Such a structure would have featured

Table 2. Interatomic Distances and Debye−Waller factors refined for the cluster with "$ZnRuO_3$" Structure within $Ru_{1-x}Zn_xO_2$ Materials Obtained by Fitting the k^3-Normalized Fourier Transformed EXAFS Function for Zn K Edge (9659 eV) X-ray Absorption Spectrum[a]

		bond length (Å)		
path	CN	$ZnTiO_3$[b]	refined	DW (Å^2)
Zn−O	3	1.956	1.98(2)	0.0093(9)
Zn−O	3	2.150	1.99(2)	0.0093(9)
Zn−Ru	1	2.910	3.10(4)	0.009(4)
Zn−Zn	3	3.020	3.23(2)	0.011(3)
Zn−O	3	3.400	3.400	0.0093(9)
Zn−Ru	3	3.4050	3.57(1)	0.008(1)
Zn−O	3	3.597	3.597	0.0093(9)
Zn−Ru	3	3.663	3.79(6)	0.016(6)
Zn−Ru	3	3.818	4.01(4)	0.016(6)
Zn−Zn	1	3.927	4.13(4)	0.011(3)

[a] *R*-factor = 0.01509, *k* range 2.0−13.15 Å^{-1}, *R* range 1−4.2 Å, amplitude = 0.671, E_0 = 0.914 eV. [b] Zn−Ti distances instead of Zn−Ru distances are presented in the case of $ZnTiO_3$ reference.

8 coordinating cations in the distance of 3.1 Å from the absorbing Zn ion, whereas the coordination shell within the distance of ~3.5 Å from the absorbing atom would contain only two coordinating cations. Such an arrangement conflicts with the assumed rutile structural model. More reasonable structural model, which would also reflect the expected tendency of Zn to cluster, may be based on structural similarity of Ru and Ti oxides. It is known that naturally abundant TiO_2 rutile often contains iron impurities, which are segregated in domains with ilmenite structure.[14] Progressive leaching of iron from such minerals leads to formation of pseudorutile structure.[15] Among these possible structures, the simulated EXAFS functions of ilmenite show strong resemblance with the experimental Zn-EXAFS data. Since $ZnRuO_3$ compound is not known, we used crystallographic data file for $ZnTiO_3$ ilmenite as a structural model in which Ti atoms were replaced with Ru. During the first refinement circle, the structure was allowed to expand isotropically to accommodate possible differences due to Ru in Ti site. Then, the full-profile refinement was carried out according to the strategy and constraints described above. The results of the refinement are summarized in the Table 2 and the corresponding theoretical EXAFS function is plotted as solid line in Figure 6 in R-space as well as in *k*-space in the inset. The very good agreement between experimental data and theoretical refined model and the reasonable values of the interatomic distances and DW factors suggest that Zn-rich domains do conform to ilmenite structure within $Ru_{1-x}Zn_xO_2$ material. The slight increase in the DW factors of Ru atoms possibly points out to partial occupancy of this site by Zn. Unfortunately, direct refinement of Ru/Zn fraction in each site was not possible, because the corresponding values correlate strongly with the displacement of metal atoms and the absolute values of the refined parameters contain large uncertainty. The increase of the DW factors may also indicate rather small size of the ilmenite domains within the rutile host. The interatomic distances in the Table 2

(13) Shannon, R. D. *Acta Crystallogr., Sect. A* **1976**, *32*, 751.
(14) Braun, E.; Raith, M. *Contrib. Mineral. Petrol.* **1985**, *90*, 199.
(15) Grey, I. E.; Reid, A. F. *Am. Mineral.* **1975**, *60*, 898.

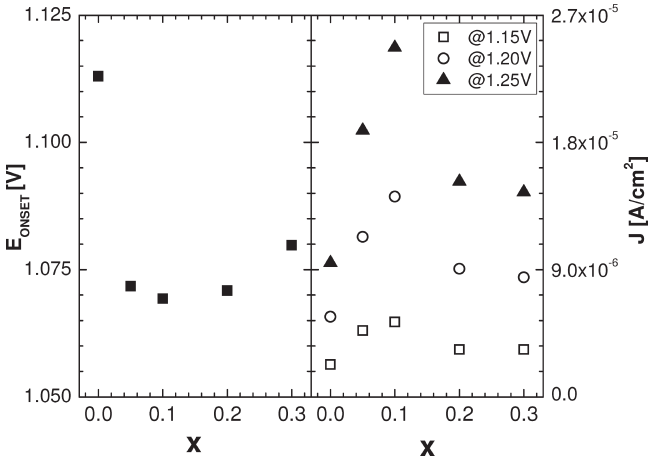

Figure 7. Current density at various potentials (right) and onsets of the oxygen evolution on $Ru_{1-x}Zn_xO_2$ electrodes in O.1 M $HClO_4$. Data were extracted from voltammetric experiments at scan rate of 5 mV/s.

show that Zn ions are located in the center of almost undistorted ZnO_6 octahedron with Zn−O distances of 1.99 Å. This value falls within the metal−oxygen distances in RuO_2 rutile of 1.93−1.99 Å (see Table 1). It is interesting to note that in the "$ZnRuO_3$" cluster the environment of Zn ion is undistorted opposite to $ZnTiO_3$,[16] which means that atomic arrangement in this $ZnRuO_3$ cluster is more isotropic compared to the bulk $ZnTiO_3$ compound. This conclusion seems to be in the agreement with the fact that all refined metal−metal distances in $ZnRuO_3$ are 0.12−0.2 Å longer than the corresponding distances in $ZnTiO_3$ bulk phase. Such an observation may look surprising because one would expect only minor differences between two structures due to the close ionic radii of Ti^{4+}(0.61 Å) and Ru^{4+}(0.62 Å).[13] Closer inspection can, however, attribute the larger than expected metal−metal distances to the effect of the RuO_2 matrix, which should generate additional strain to accommodate the defects in the atomic packing of rutile. One should also notice that formation of the clusters with the ilmenite structure could be a natural mechanism to compensate for the anticipated oxygen nonstoichiometry when divalent Zn ions are placed into the rutile lattice instead of tetravalent Ru ions. Such a mechanism of oxygen deficiency accommodation may be of a general character for the combination of divalent cation in tetravalent oxide because ilmenite inclusions were also reported for the Co-doped TiO_2 anatase films[17] in which the oxidation state of Co was determined to be +2.

The electrocatalytic activity and selectivity of the $Ru_{1-x}Zn_xO_2$ materials in OER and CER processes are summarized in Figures 7−9. In the case of oxygen evolution in acid media, i.e. in absence of chlorides, (see Figure 7) one observes qualitatively similar behavior on $Ru_{1-x}Zn_xO_2$ and nondoped RuO_2. The activity of Zn-doped materials is slightly higher than that of nondoped material as it is shown by both current density and onset of the anodic current. The activity toward oxygen

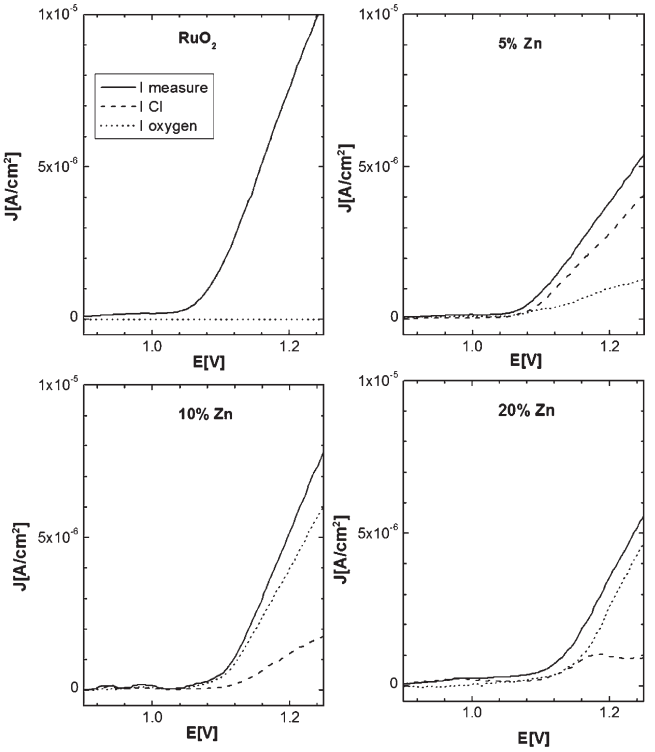

Figure 8. Measured current and DEMS based oxygen and chlorine contributions for parallel oxygen and chlorine evolution processes on $Ru_{1-x}Zn_xO_2$ in 0.1 M $HClO_4$/0.3 M NaCl electrolyte solution. Data were collected in voltammetric experiment at 5 mV/s.

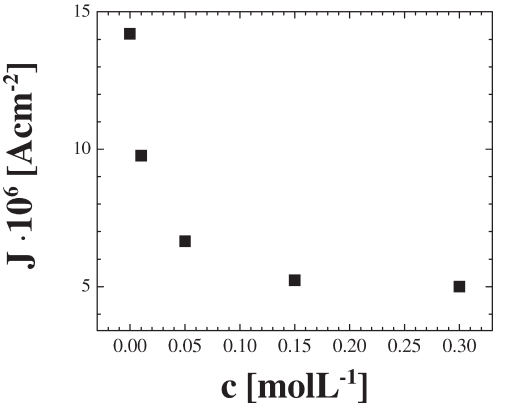

Figure 9. Chloride concentration effect on the total electrocatalytic activity of $Ru_{0.8}Zn_{0.2}O_2$ in parallel oxygen and chlorine evolution. The total electrocatalytic activity is represented by current density at 1.2 V(Ag/AgCl). Data were extracted from voltammetric experiments at 5 mV/s.

evolution shows nonmonotonous dependence on Zn content with a weak maximum at $x = 0.1$.

The selectivity of the $Ru_{1-x}Zn_xO_2$ catalysts can be assessed by combination of voltammetry with mass spectrometric detection of the reaction products. The raw data were converted into corresponding current contributions as described in ref [7,9] and are plotted in Figure 8. As follows from the Figure 8, both activity and selectivity of the $Ru_{1-x}Zn_xO_2$ catalysts are affected by the total amount of incorporated Zn ions. The pure (i.e., nonsubstituted) RuO_2 shows higher activity in parallel OER and CER than Zn doped materials. Also the onset of the anodic current shows

(16) Bartram, S. F.; Slepetys, A. *J. Am. Ceram. Soc.* **1961**, *44*, 493.
(17) Shimizu, N.; Sasaki, S.; Hanashima, T.; Yamawaki, K.; Udagawa, H.; Kawamura, N.; Suzuki, M.; Maruyama, H.; Murakami, M.; Matsumoto, Y.; Koinuma, H. *J. Phys. Soc. Jpn.* **2004**, *73*, 800.

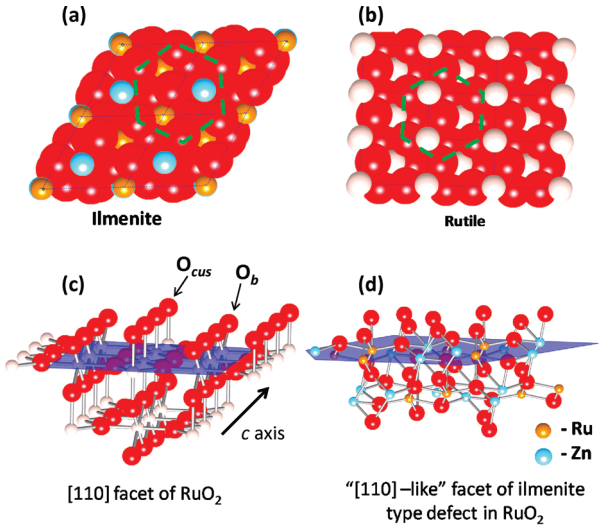

Figure 10. Arrangement of atoms in terms of atomic close packing in (a) ilmenite and (b) rutile and the corresponding catalytically active surfaces of (c) rutile and (d) ilmenite.

pronounced shift to higher potentials suggesting the anodic gas evolution becomes more hindered on materials with higher Zn content. This trend in the overall catalytic activity is opposite to that for the simple oxygen evolution (see above). A decrease in the overall activity has not been observed also for the other ruthenium oxides with heterovalent substitution.[7,9] The dependence of the $Ru_{1-x}Zn_xO_2$ catalysts activity on Zn content in parallel OER and CER remains the same as in the case of simple oxygen evolution. The drop in the overall activity is, however, accompanied by the significant shift of the selectivity toward oxygen evolution (see Figure 8), which increases with increasing Zn content. The overall activity as well as selectivity toward oxygen evolution in parallel OER and CER evolution decreases with increasing chloride concentration (see Figure 9).

The general trends in the electrocatalytic behavior of $Ru_{1-x}Zn_xO_2$ catalysts can be rationalized in terms of the changes of the local structure resulting from Zn doping. Because the EXAFS data do not suggest any abrupt changes in the character of Zn distribution, we may assume the ilmenite type blocks are distributed evenly in the crystallites in the whole range of Zn concentrations. Moreover, the size of such domains should be quite small because they do not yield any additional reflections in the X-ray and electron diffraction patterns. To understand the effect of Zn clustering on the change of selectivity in the electrocatalytic chlorine/oxygen evolution, we should recollect the similarities and the differences between ilmenite and rutile lattices. The crystal structure of ilmenite can be described in terms of the hexagonal close packing of oxygen ions, whereas Ru and Zn atoms occupy octahedral voids forming separate layers as shown in Figure 10a, which presents the view of the lattice perpendicular to $a-b$ plane. As follows from the stoichiometry, each Zn atom involves one Ru atom into the formation of "$ZnRuO_3$" ilmenite block. Concerning the rutile structure, it has similar type of oxygen packing (see Figure 10b). Significant difference between both structural types (apart from the distortion of oxygen planes) is connected with the cation arrangement, which follows a slightly different sequence in the rutile than in ilmenite. Keeping in mind the structure of the theoretically predicted active site for anodic gas evolution, which is fundamentally affected by cation arrangement, one can view the different cation stacking in ilmenite as the primary reason of different electrocatalytic behavior of Zn doped RuO_2 materials. It can be visualized by extrapolation of the Zn-rich ilmenite structural block from bulk of a nanoparticle to its surface. Figure 10c presents the atoms arrangement on the catalytically active (110) facet of RuO_2. The rutile type surfaces expose the facets with cations stacked along c axis (bonding distance of ca. 3.1 Å) coordinated alternatively with either bridging oxygen atoms (O_b) or coordination unsaturated oxygen atoms (O_{cus}) where each type of coordinating oxygen is also ordered along the c axis. This type of the arrangement is favorable for the formation of surface confined peroxo species out of two neighboring O_{cus}, and is in principle essential for both OER and CER processes.[4,5] The corresponding ilmenite type surfaces, when exposed as a part of the intergrowth, do not allow for such cation stacking (see Figure 10d). They feature random distribution of both types of coordinating oxygen atoms (O_b and O_{cus}) on the surface. The formation of surface peroxo groups is, therefore, structurally hindered because O_{cus} atoms are separated too far apart. It blocks the main reaction pathway of both considered processes oxygen and chlorine evolution.[4,5] In addition to this structural effect, the formation of ilmenite type inclusions can be intuitively perceived as formation of a defect facilitating the oxygen surface diffusion.

The structural hindrance of the main oxygen and chlorine evolution mechanisms should generally lead to a decrease of electrocatalytic activity of the $Ru_{1-x}Zn_xO_2$ electrocatalysts compared to nondoped RuO_2. In a similar manner, the activity of the Zn doped materials should decrease with increasing Zn content. These predictions, based on the theoretically posed reaction mechanisms, active sites and EXAFS based structural model of $Ru_{1-x}Zn_xO_2$ phases, can be used to rationalize the trends observed in parallel oxygen and chlorine evolution, but fail to describe the behavior observed for oxygen evolution in the absence of chlorides.

The increase of the activity in OER connected with Zn doping suggests a presence of an alternative oxygen evolution mechanism accompanying the main peroxo route. Crystal edge facilitated recombination of surface confined oxo species[6] can be viewed as such an alternative mechanism. This reaction path, which has not been involved in the DFT calculations,[4,5] anticipates that the oxo-species generated electrochemically on the crystal facets need to be transported to the crystal edges to form the oxygen molecule. The actual $Ru_{1-x}Zn_xO_2$ catalysts are likely to feature both types of surfaces discussed above. One may expect the overall oxygen evolution activity to contain two contributions – oxygen formation via peroxo mechanism on rutile type (Zn abated) blocks and recombination mechanism on ilmenite blocks (Zn-rich). The observed OER related activity should increase as long as the recombination mechanism compensates for the loss of rutile type surface fraction

producing the oxygen via the main peroxo-based route. This condition applies in the range of $0 < x < 0.1$ where the ilmenite type surface involves less than 20% of the cations.

In the case of parallel oxygen and chlorine evolution one has to expect that not only oxygen but also chlorine may be evolved by more than one mechanism due to the coexistence of rutile and ilmenite surfaces. The usual CER mechanism, which starts by Cl^- attack of the surface peroxo groups,[5] is confined to rutile type surface and does not apply to ilmenite type surfaces where these peroxo groups do not form and a recombination mechanism (probably similar to that of oxygen) will be prevailing.[18] It has to be stressed, however, that coexistence of recombination assisted oxygen and chlorine evolution on ilmenite type surface should decrease partial current density of each of the processes due to lower probability of the successful recombination to gaseous products. This should result also in a drop of the total electrocatalytic activity with increasing Zn content. This trend is mitigated by presence of the rutile type structural blocks in materials with overall Zn content lower than 10%, but is clearly manifested by the shift of the onset of electrocatalytic current to higher potentials with increasing Zn content. The available selectivity data suggest that significant improvement of the selectivity is accompanied by suppression of the electrocatalytic activity of the rutile blocks because the recombination mechanism seems to favor oxygen evolution over that of chlorine and eventually may lead to potential independent chlorine evolution.

(18) Erenburg, R. G.; Krishtalik, L. I.; Bystrov, V. I. *Elektrokhymiya* **1972**, *8*, 1602.

Conclusions

Zn cations substitution into the crystal lattice of RuO_2 leads to the formation of a metastable material composed of Ru-rich blocks intergrowing with Zn enriched domains of ilmenite structure. Although the Ru-rich rutile blocks retain the electrocatalytic activity predicted theoretically, the blocks with ilmenite structure change the selectivity of the resulting materials toward oxygen evolution. The ilmenite structure features different cation arrangement with respect to that of rutile particularly within catalytically active (110) facet. It hinders the formation of surface confined peroxo species, which play an essential role in both oxygen and chlorine evolution reactions on conventional rutile type oxides.

Acknowledgment. This work was supported by the Grant Agency of the Academy of Sciences of the Czech Republic under Contracts IAA400400906 and M200400902. V.P. acknowledges the support of the Marie Curie International Incoming Fellowship (IIF 220711) of the European Commission. The synchrotron measurement time was provided by National Synchrotron Light Source at Brookhaven National Laboratory Project 11734.

Supporting Information Available: Thermogravimetric analysis data, flowchart of synthesis procedures, RuK edge XANES data (PDF). This material is available free of charge via the Internet at http://pubs.acs.org.